Research Square

Preprints are preliminary reports that have not undergone peer review.
They should not be considered conclusive, used to inform clinical practice,
or referenced by the media as validated information.

Reconciling Discrepancies Between Observed and Model-Simulated Cloud Radiative Trends and Their Implications for Earth's Energy Imbalance

Chanyoung Park

chanyoung.park@miami.edu

University of Miami https://orcid.org/0000-0001-8644-1031

Brian Soden

University of Miami https://orcid.org/0000-0001-9693-8236

Research Article

Keywords:

Posted Date: April 28th, 2026

DOI: https://doi.org/10.21203/rs.3.rs-9054442/v2

License: This work is licensed under a Creative Commons Attribution 4.0 International License.
Read Full License

Additional Declarations: The authors declare no competing interests.

Reconciling Discrepancies Between Observed and Model-Simulated Cloud Radiative Trends and Their Implications for Earth's Energy Imbalance

Chanyoung Park[1]*, Brian J. Soden[1]

[1] Rosenstiel School of Marine, Atmospheric, and Earth Science, University of Miami, Miami, FL, USA.

*Corresponding author: Chanyoung Park (chanyoung.park@miami.edu)

Key Points:

- Observed cloud radiative trends using two methods agree on the spatial pattern but show near-uniform residuals with opposite SW and LW signs
- Multiple diagnostics suggest that the observed residuals are consistent with satellite instrumentation drift
- Offsetting SW and LW biases result in robust net trends, but explain the discrepancies between observed and model-simulated radiative trends

Abstract

Satellite observations over the past two decades show increased shortwave (SW) absorption and outgoing longwave (LW) radiation at the top of the atmosphere (TOA), changes that have been interpreted as evidence of substantial cloud radiative contributions to the recent rise in Earth's energy imbalance (EEI). However, climate models reproduce only part of the observed trends. Here, we use an independent cloud radiative kernel (CRK) framework to re-evaluate the observed SW and LW cloud radiative trends over 2003–2022. The CRK-based estimates reproduce the observed spatial patterns and temporal variability, but explain only a fraction of the global-mean trend magnitudes, leaving spatially coherent residuals that are difficult to reconcile with known physical mechanisms. In contrast, CMIP6 historical simulations show broad agreement with CRK-based cloud radiative trends across multiple independent 20-year periods, with no evidence of near-uniform residuals. We further examine several independent diagnostics of radiometric stability, including trends in the cloud radiative kernel itself, albedo changes over three invariant Earth targets, and daytime-minus-nighttime differences in longwave and window-channel TOA fluxes. Together, these diagnostics consistently suggest subtle but statistically significant long-term drift in the CERES radiative record. These results suggest that most of the discrepancy between observed and simulated SW and LW trends arises from this observational drift. However, the offsetting nature of the SW and LW biases leaves the inferred net radiative contribution to EEI comparatively robust.

Plain Language Summary

Satellite observations over the past two decades show that Earth is absorbing more sunlight and emitting more heat to space. These changes have been interpreted as evidence that clouds contributed substantially to the recent rise in Earth's energy imbalance. However, climate models simulate smaller cloud-related trends than satellite-based estimates, creating an apparent gap between models and observations. To investigate this mismatch, we applied an independent method called a cloud radiative kernel framework. Although this method reproduces the observed spatial patterns, it yields smaller global-mean trends in both shortwave and longwave fluxes. The remaining difference is spatially uniform, which is difficult to explain by real cloud changes alone. We further examined several independent tests of satellite radiometric stability, including trends in the cloud radiative kernel, reflectance changes over three stable Earth targets, and differences between daytime and nighttime radiation measurements. Together, these tests indicate subtle but significant long-term drift in the satellite record. Our results suggest that the discrepancies between observed and simulated cloud radiative trends may arise from these observational drifts. At the same time, because the shortwave and longwave biases offset one another, the recent increase in Earth's energy imbalance appears to remain relatively robust.

1. Introduction

The Earth's energy imbalance (EEI)—the difference between absorbed solar radiation and outgoing terrestrial radiation—has increased markedly over the past two decades, driving accelerated warming of the global climate system (e.g., von Schuckmann et al., 2016; Loeb et al., 2021; Mauritsen et al., 2025). Observations from the Clouds and the Earth's Radiant Energy

System (CERES) show that this increase reflects increase in both absorbed shortwave (SW) and outgoing longwave (LW) radiation at the top of the atmosphere (TOA), with enhanced absorption of SW radiation playing the dominant role in the net trend (e.g., Kramer et al., 2021; Loeb et al., 2021; Raghuraman et al., 2021; Stephens et al., 2022; Goessling et al., 2025; Park and Soden, 2025). Given the distinct physical processes governing SW and LW radiation, quantifying the drivers of these TOA flux changes is essential for disentangling the roles of anthropogenic forcing and climate feedbacks and for constraining climate sensitivity.

Radiative kernels are widely used for this purpose because they provide a physically transparent way to decompose TOA radiative changes into contributions from individual drivers. In this framework, precomputed local linear sensitivities ("kernels") translate small perturbations in well-defined surface and atmospheric state variables—such as surface albedo, water vapor, and temperature—into their associated radiative flux changes. Clouds, however, do not fit into this linear framework as they are not represented by a simple state variable, and their radiative influence depends jointly and nonlinearly on cloud fraction, height, optical thickness, and vertical overlap (Soden and Held, 2006; Soden et al., 2008). Consequently, standard radiative kernel approaches do not provide an explicit cloud kernel, motivating alternative strategies for diagnosing cloud-driven radiative responses. One common approach is an "*adjustment*" method, in which observed changes in cloud radiative effect (CRE) are corrected for the kernel-estimated radiative impacts of contemporaneous non-cloud perturbations in the state variables, thereby accounting for cloud masking effects and indirectly isolating the true cloud contribution (e.g., Soden et al., 2008; Kramer et al., 2021). We refer to this quantity as the adjusted, or adjustment-based, cloud radiative response, dR_{cld}-Adj.

Observationally derived adjustment estimates indicate substantial cloud radiative contributions to the recent TOA flux trends. Raghuraman et al. (2023) showed that, over 2001–2020, the trend in the observed shortwave cloud radiative response, dSW_{cld}-Adj, is 0.39 ± 0.20 W m^{-2} decade^{-1} (95% confidence), implying that cloud changes account for ~61% of the observed increase in absorbed shortwave radiation. In the longwave, the observed cloud radiative trend, dLW_{cld}-Adj, is −0.27 W m^{-2} decade^{-1} (95% confidence), indicating that clouds offset part of the shortwave warming through enhanced longwave emission to space. Climate models, however, reproduce only part of this observed behavior. In the same study, prescribed sea surface temperature and sea-ice simulations yielded a multi-ensemble mean trend of 0.24 W m^{-2} decade^{-1} in dSW_{cld}-Adj, capturing only about 60% of the central observational estimate and lying near the lower bound of the observational uncertainty range. The discrepancy is even larger in the longwave, where the multi-ensemble mean dLW_{cld}-Adj trend is 0.01 W m^{-2} decade^{-1}, placing the model-derived value well outside the observational uncertainty range. Thus, relative to the observations, models underestimate the positive shortwave cloud radiative trend and fail to reproduce the compensating negative longwave trend, motivating further investigation into the source of this discrepancy.

To assess whether the model–observation gap in cloud radiative trends arises from differing cloud changes or from limitations of the adjustment approach, we evaluate dR_{cld}-Adj using an independent diagnostic—the cloud radiative kernel (CRK) framework. The CRK is defined in a 7 × 6 space (or, in some implementations, 7 × 7) of cloud top pressure (CTP) and cloud optical depth (COD) and provides the TOA radiative sensitivity to changes in cloud fraction within each cloud type bin (Rossow and Schiffer 1999; Zelinka et al., 2012a; Zhou et al., 2013; Yue et al., 2016;

Zhang et al., 2021; Sun et al. 2022). Because each bin uniquely represents a combination of cloud height, thickness, and associated radiative properties, multiplying the CRK by changes in cloud fraction implicitly accounts for the radiative responses of cloud amount, cloud altitude, and cloud optical thickness simultaneously (Zelinka et al., 2012a,b; Zelinka et al., 2016). In this sense, the CRK framework represents the full radiative response of clouds expressed through changes in the distribution of cloud scenes in CTP–COD space.

Conceptually, the adjustment and CRK frameworks target the same quantity—the TOA radiative response to cloud changes—so their global-mean trends should agree within uncertainty if both methods faithfully represent cloud-driven radiative changes. However, our analysis finds a clear disagreement between these two approaches in observations. Although the CRK-based estimates (dR_{cld}-CRK) reproduce the spatial patterns of the adjusted trends, they explain only part of the global-mean trends in dR_{cld}-Adj. Moreover, the residuals (dR_{cld}-Adj minus dR_{cld}-CRK) are spatially coherent, being positive in the shortwave and negative in the longwave over much of the globe. This behavior contrasts with the pronounced regional structure expected from physically driven cloud changes and suggests that part of the apparent model–observation discrepancy may instead reflect observational uncertainty. Taken together, these findings highlight the need for careful interpretation when attributing long-term cloud radiative changes from satellite records.

2. Data

We use monthly mean radiative fluxes from the CERES Energy Balanced and Filled (EBAF) Edition 4.2 product (Loeb et al., 2018) and the FluxByCldTyp Edition 4.1 (FBCT) dataset (Sun et al., 2022) for January 2003–December 2022. Over this period, FBCT is derived exclusively from

Terra and Aqua observations, allowing cloud radiative diagnostics to be interpreted without complications arising from changes in satellite platforms (Text S1). We also use the CERES Single Scanner Footprint (SSF) Edition 4 dataset, which provides the primary footprint-level input to FBCT, to derive albedo diagnostics over three invariant Earth targets and to examine day-minus-night differences in longwave and window-channel fluxes as independent tests of long-term radiometric stability. For both Terra and Aqua, only observations obtained in cross-track mode are used, consistent with standard CERES processing practice.

To provide a controlled consistency check, we estimate dR_{cld}-Adj and the dR_{cld}-CRK in Coupled Model Intercomparison Project Phase 6 (CMIP6) historical simulations, where radiative fluxes and cloud properties are internally consistent and unaffected by satellite sampling or calibration uncertainties. We analyze 14 models that provide the variables required to compute both estimates (Table S1). To place these results in the broader context of Earth's energy imbalance over 2003-2022, we additionally use 44 CMIP6 models for analyses based on the adjustment method alone, for which the necessary variables are available (Table S1).

Cloud radiative diagnostics are evaluated on a global 2.5° × 2.5° latitude–longitude grid to facilitate spatially resolved trend analysis while maintaining adequate sampling across cloud regimes in CTP–COD space. All other gridded fields are retained at their original 1° × 1° resolution.

3. Materials and Methods

3.1. Radiative Kernel Framework

Radiative kernels, originally introduced by Soden and Held (2006), are precomputed radiative sensitivities that quantify how TOA fluxes respond to small perturbations in well-defined climate state variables such as surface albedo, water vapor, and temperature. For a given non-cloud variable x, the all-sky TOA radiative response dR_x is approximated as

$$\mathrm{dR}_x = \frac{\partial \mathrm{R}}{\partial x}\mathrm{d}x = K_x \mathrm{d}x, \qquad (1)$$

where K_x is the radiative kernel (all-sky TOA flux change associated with a small perturbation in x) and $\mathrm{d}x$ is the actual anomaly in state variable x. Clear-sky radiative responses are estimated analogously using clear-sky kernels, yielding $\mathrm{dR}_x^{\mathrm{clr}} = K_x^{\mathrm{clr}}\,\mathrm{d}x$.

These relationships form the basis of the adjustment method. We express the adjusted cloud radiative response, $\mathrm{dR}_{\mathrm{cld}}$-Adj, as

$$\mathrm{dR}_{\mathrm{cld}}\text{-Adj} = \mathrm{dCRE} - \left\{\sum_x \left(\mathrm{dR}_x - \mathrm{dR}_x^{\mathrm{clr}}\right) + \left(\mathrm{IRF} - \mathrm{IRF}^{\mathrm{clr}}\right)\right\}, \qquad (2)$$

where dCRE is the anomaly in cloud radiative effect, defined as the difference between all-sky and clear-sky TOA flux anomalies (downward positive). The bracketed term represents the cloud-masking correction associated with contemporaneous non-cloud perturbations, reflecting that

changes in non-cloud variables affect all-sky and clear-sky fluxes differently in the presence of clouds. Here, IRF and IRF^{clr} are the all-sky and clear-sky instantaneous radiative forcing, respectively. In the radiative kernel framework, IRF^{clr} is diagnosed as the clear-sky residual, that is, the portion of the clear-sky radiative change not explained by the surface albedo, water vapor, and temperature kernel terms. The all-sky forcing, IRF, is then estimated by scaling this clear-sky residual to account for cloud masking. In practice, the physical interpretation of this term differs between the SW and LW, representing primarily aerosol direct effects in the SW and well-mixed greenhouse gas forcing, especially CO_2, in the LW (Kramer et al., 2021).

As an independent benchmark for evaluating radiative-kernel-based adjustment estimates of cloud radiative responses, we also use the partial radiative perturbation (PRP) estimate based on CERES EBAF Edition4.2.1 provided by Loeb et al. (2025). In the PRP framework, individual non-cloud contributors to TOA radiative flux (e.g., surface albedo, water vapor, temperature, aerosols, trace gases, and solar irradiance) are perturbed one at a time within a radiative transfer model while all other components are held fixed (Wetherald and Manabe, 1988; Thorsen et al., 2018). This approach directly diagnoses the radiative impact of each perturbation without relying on a linear approximation about a reference state. It is important to note that in both the radiative-kernel and PRP frameworks, “aerosol effects” refer to aerosol–radiation interactions (direct scattering and absorption of sunlight), not aerosol–cloud microphysical interactions, which are implicitly included in the cloud contribution.

In this study, we use radiative kernels from the CloudSat/CALIPSO-derived observational framework of Kramer et al. (2019). Radiative fluxes at the TOA are taken from the CERES FBCT

Edition 4.1 product (Sun et al., 2022). Surface albedo is taken from CERES EBAF Edition 4.2 (Loeb et al., 2018). Specific humidity and temperature profiles are obtained from the ERA5 reanalysis (Hersbach et al., 2020), and surface temperature from GISTEMP v4 (Lenssen et al., 2019).

3.2. Cloud Radiative Kernel Framework

Cloud radiative kernels (CRKs) provide a CTP–COD histogram framework, representing the TOA radiative response to a 1% change in cloud fraction within each cloud type (Zelinka et al., 2012a; Zhou et al., 2013; Yue et al., 2016; Zhang et al., 2021; Sun et al. 2022).

In the CERES-FBCT implementation, CRKs are provided on a 7 × 6 CTP–COD binning and are derived from sub-footprint radiative transfer calculations using MODIS cloud retrievals collocated with CERES radiances (Sun et al., 2022). The CRK for each CTP–COD bin is defined as the difference between the overcast-sky TOA flux for that cloud type and the corresponding clear-sky TOA flux (downward positive), normalized by 100% cloud fraction, $(\mathrm{R}^{\mathrm{ovc}} - \mathrm{R}^{\mathrm{clr}})/100\%$ (units: W m^{-2} $\%^{-1}$). In this study, we use the 2003–2022 climatological mean kernels. The annual-mean, global-mean shortwave (SWCRK) and longwave (LWCRK) cloud radiative kernels are shown in Fig. S1.

In this framework, the cloud radiative response in each cloud-type bin is estimated as the product of the cloud radiative kernel and the change in cloud fraction:

$$\mathrm{dR_{cld}\text{-}CRK}_i = \mathrm{CRK}_i \times \mathrm{dCF}_i, \qquad (3)$$

where CRK_i is the cloud radiative kernel for cloud type i, dCF_i is the cloud fraction anomaly, and i indexes the 42 CTP–COD bins. Because the kernels are computed under climatological atmospheric and surface conditions, the resulting radiative changes are attributable solely to changes in cloud fraction and do not include clear-sky radiative changes (Zelinka et al., 2012a). Summing over all bins yields the total $\mathrm{dR_{cld}}$-CRK, which are then compared with the corresponding adjustment-based estimates.

We also use the Zhou et al. (2013) cloud radiative kernels (hereafter Z13) as an alternative to support the robustness of our results (Text S2). Z13 computed kernels on a 7 × 7 CTP–COD space using zonal-mean temperature, humidity, and ozone profiles from ERA-Interim over 2000–2010 and radiative transfer calculations applied to an ISCCP-like CTP–COD discretization. The SWCRK was first calculated for discrete surface-albedo bins and then mapped to individual grid cells using CERES EBAF Edition 4.2 surface albedo, yielding a spatially varying shortwave kernel. In contrast, the LWCRK was spatially expanded from a zonal-mean kernel. Because FBCT reports cloud properties only for optical depths greater than 0.25, owing to larger retrieval uncertainties for very thin clouds (Minnis et al., 2011; Sun et al. 2022), we omit the thinnest COD bin (0–0.3) from the Z13 CRKs and use six COD bins for consistency with FBCT. Excluding this bin has been shown to have a negligible impact on cloud feedback estimates and is therefore unlikely to affect the trend estimates examined here (Chao et al., 2024).

3.3. CMIP6 Analysis

For consistency with the observational analysis, we use the same CloudSat/CALIPSO radiative

kernels introduced by Kramer et al. (2021) to compute dR_{cld}-Adj. We estimate dR_{cld}-CRK using the cloud radiative kernels derived from CERES FBCT (Sun et al., 2022) together with model-simulated cloud fraction resolved in CTP–COD space. In addition, we apply the independent CRK formulations of Z13 to assess the robustness of the results to kernel choice.

To ensure statistical independence and to sample a wide range of forcing environments, we compute linear trends over nine non-overlapping 20-year periods. Eight periods are drawn from the historical simulations spanning 1855–2014, encompassing intervals with varying greenhouse gas forcing, aerosol loading, and volcanic influences. An additional period covering 2003–2022 is constructed using concatenated historical through 2014 and SSP2-4.5 simulations for 2015–2022, thereby matching the observational record. Only three models (GFDL-CM4, HadGEM3-GC31-LL, and IPSL-CM6A-LR) provide the necessary variables for this recent period. The use of multiple independent 20-year segments allows the relationship between dR_{cld}-Adj and dR_{cld}-CRK to be assessed across diverse climatic states and forcing conditions.

For the CMIP6 analysis based on the FBCT-derived CRKs, an additional preprocessing step is required because the FBCT kernels are defined only where the corresponding observed cloud-type information is available, leaving missing values in some grid cells. To produce a spatially complete kernel fields and make the FBCT-based analysis directly comparable to the Z13 CRKs, we first fill missing values using the zonal-mean kernel at the same latitude. In the few cases where missing values remain within individual CTP–COD bins, we further infill them using CTP-mean kernel values at the same COD for the shortwave and COD-mean kernel values at the same CTP for the longwave. This approach is motivated by the fact that the SWCRK depends primarily on COD and

is relatively insensitive to CTP, whereas the LWCRK depends primarily on CTP and is relatively insensitive to COD (Fig. S1). This infilling approach preserves the large-scale spatial structure of the kernels while avoiding artificial discontinuities associated with missing grid cells.

3.4. Albedo Diagnostics Over Invariant Earth Targets

To evaluate radiometric stability in CERES observations, we examine three widely used invariant Earth targets: deep convective clouds (DCCs), Libya-4, and Dome C. DCCs are commonly used as a benchmark for long-term satellite stability tests because they are optically thick, highly reflective, nearly Lambertian targets with relatively small natural variability and weak sensitivity to lower-tropospheric aerosol perturbations. Libya-4 and Dome C are also widely used invariant surface targets in calibration studies: Libya-4 is a bright, spatially homogeneous desert target, while Dome C is a stable high-albedo snow surface over Antarctica.

Following Shankar et al. (2023), we identify DCCs in CERES SSF using strict selection criteria. A footprint is classified as a DCC target if it satisfies all of the following: (1) ocean surface; (2) 30°S–30°N; (3) mean cloud top temperature < 205 K; (4) viewing zenith angle < 40° and solar zenith angle < 40°; (5) 100% cloud fraction; and (6) filtered window-channel radiance < 1 W m^{-2} sr^{-1} μm^{-1}. These criteria are intended to minimize contamination from thin cirrus, mixed cloud scenes, and angular effects while retaining the most radiometrically stable DCC targets.

For the surface targets, we use Libya-4 centered near 28.5°N, 23.4°E and Dome C centered near 75.1°S, 123.4°E. In each case, targets are selected from CERES footprints falling within an approximately 20 km × 20 km box centered on the site under clear-sky conditions and with viewing

zenith angle < 40°. For Dome C, an additional solar zenith angle constraint of < 80° is applied. For high-resolution imagers such as MODIS, calibration studies over Libya-4 and Dome C often apply an explicit bidirectional reflectance distribution function (BRDF) correction to account for angular reflectance variations (Wu et al., 2013; Doelling et al., 2015). In CERES SSF, however, the reported TOA fluxes are obtained from measured radiances using CERES angular distribution models (ADMs). We therefore use the CERES TOA flux product directly, while noting that these ADMs are scene-type-based anisotropy corrections rather than site-specific BRDF models for Libya-4 or Dome C.

For all three targets, albedo is computed from the filtered footprint set as

$$\alpha_{\mathrm{target}} = \frac{M_{\mathrm{SW}}}{\mu_0 S_0}, \qquad (4)$$

where M_{SW} is the TOA reflected shortwave flux, $\mu_0 = \cos(\theta_0)$, θ_0 is the solar zenith angle, and S_0 is the incident solar irradiance at the TOA (≈1361 W m^{-2}) from the Total Irradiance Monitoring instrument on SORCE or TSIS (Shankar et al., 2023). Footprint-level α_{target} values are then aggregated to monthly means to quantify target variability and long-term trends. For Dome C, annual means are used instead of monthly means because polar night prevents year-round sampling.

3.5. Longwave and Window-Channel TOA Fluxes: Daytime-minus-Nighttime Differences

Trends in the daytime-minus-nighttime differences in LW and window (WN) TOA radiative fluxes, $\left(\mathrm{LW}_{\mathrm{day}} - \mathrm{LW}_{\mathrm{night}}\right) - \left(\mathrm{WN}_{\mathrm{day}} - \mathrm{WN}_{\mathrm{night}}\right)$, provide a diagnostic of possible drifts in the SW

channel or in the SW component of the total (TOT) channel (Loeb et al., 2012; Loeb et al., 2016). This diagnostic is based on the fact that nighttime LW radiances are measured directly from the TOT channel, whereas daytime LW radiances are inferred from the difference between the TOT and SW channels. Because daytime LW flux depends on separating the SW contribution from the TOT signal, any calibration drift in the SW channel, or error in the SW correction applied to the TOT channel, can introduce artificial trends in the inferred daytime LW flux. Such artifacts may appear as spurious long-term changes in the daytime-minus-nighttime LW contrast. The WN channel provides an additional, largely independent constraint because it primarily measures thermal emission in the atmospheric window region and therefore captures changes in the diurnal cycle of longwave radiation. Differences between LW and WN day-minus-night contrasts can thus be used to assess whether apparent LW changes reflect true geophysical variability or instead arise from possible long-term radiometric drift.

Using CERES SSF data, we separate daytime and nighttime TOA fluxes and aggregate them onto monthly $1^\circ \times 1^\circ$grids. We then analyze monthly anomalies in the daytime-minus-nighttime LW and WN fluxes and their linear trends over 2003–2022.

4. Results

4.1. Discrepancies in Observed Cloud Radiative Trends

Figure 1 shows the spatial distributions of the linear trends in the cloud radiative response, dR_{cld}, over 2003–2022. Overall, the adjustment-based estimate, dR_{cld}-Adj, and the cloud radiative kernel estimate, dR_{cld}-CRK, exhibit remarkably similar spatial structures. In the shortwave, both methods capture the major regional features, with a spatial correlation of $r = 0.94$ ($p < 0.001$).

A similarly strong correspondence is found in the longwave, with a spatial correlation of $r = 0.88$ ($p < 0.001$). After removing the linear trends, the detrended global-mean monthly anomalies also remain highly correlated in both the shortwave and longwave ($r = 0.92$ and $r = 0.88$, respectively; both $p < 0.001$), indicating that the two independent frameworks capture similar temporal variability as well.

Despite this strong agreement in spatial structure and temporal variability, the global-mean trends differ substantially between the two methods. In the shortwave, the trend in dSW_{cld}-Adj is 0.413 ± 0.106 W m^{-2} decade^{-1}, whereas the corresponding trend in dSW_{cld}-CRK is 0.139 ± 0.099 W m^{-2} decade^{-1} (95% confidence), accounting for only about one-third of the dSW_{cld}-Adj trend. A similarly pronounced discrepancy is found in the longwave. The trend in dLW_{cld}-Adj is –0.283 ± 0.076 W m^{-2} decade^{-1}, compared with –0.047 ± 0.061 W m^{-2} decade^{-1} for dLW_{cld}-CRK (95% confidence). Thus, the discrepancy between the two approaches arises primarily from differences in global-mean trend magnitude rather than from differences in the regional structure or temporal variability of the cloud radiative response.

This difference is seen more clearly in Fig. 1c,f, which show the residual trends defined as dR_{cld}-Adj minus dR_{cld}-CRK. The residuals exhibit a near-uniform positive signal in the shortwave and a corresponding negative signal in the longwave over much of the globe, particularly over the oceans. Their global-mean magnitudes are substantial, reaching 0.275 W m^{-2} decade^{-1} in the shortwave and −0.236 W m^{-2} decade^{-1} in the longwave, and in both cases exceeds the magnitude of the CRK-based trends. Compared with the shortwave residual, the longwave residual appears somewhat more spatially heterogeneous, likely reflecting the greater sensitivity

of longwave cloud radiative responses to uncertainty in non-cloud contributions, especially those associated with water vapor and temperature. By contrast, shortwave non-cloud contributions from surface albedo and water vapor are relatively small. Nevertheless, the residuals remain spatially coherent on global scales. This behavior is difficult to reconcile with physically driven cloud changes alone, which would be expected to produce stronger regional structure.

To assess whether this discrepancy could instead reflect uncertainty in the radiative-kernel-based adjustment framework, we compare dR_{cld}-Adj with an independent estimate derived from the PRP framework (Fig. S2). The two adjustment-based estimates exhibit highly consistent interannual variability and long-term trends, both indicating increased absorption of solar radiation and reduced emission of terrestrial radiation associated with cloud changes. In the shortwave, the trend in dSW_{cld}-Adj is 0.413 ± 0.106 W m^{-2} $decade^{-1}$ using radiative kernels and 0.412 ± 0.116 W m^{-2} $decade^{-1}$ using PRP (95% confidence). In the longwave, the corresponding trends are −0.283 ± 0.076 W m^{-2} $decade^{-1}$ and −0.223 ± 0.062 W m^{-2} $decade^{-1}$. This close agreement indicates that the adjustment-based estimate is robust across CERES products and across distinct approaches for accounting for non-cloud radiative contributions (i.e., radiative kernel vs PRP).

This interpretation, however, comes with an important caveat. dR_{cld}-Adj is not a directly observed quantity. Rather, it is diagnosed as a residual by removing cloud-masking effects associated with non-cloud perturbations from dCRE. The adjustment framework therefore assumes that non-cloud contributions are accurately isolated and removed and that the underlying observed dCRE trends are sufficiently stable. Any uncertainty in the radiative flux record can therefore project directly onto the inferred dR_{cld}-Adj. The near-uniform residuals in Fig. 1c,f, together with the residual

nature of the adjustment estimate itself, therefore motivate a set of consistency checks to determine whether the mismatch reflects expected methodological differences or unresolved uncertainty in the observational record.

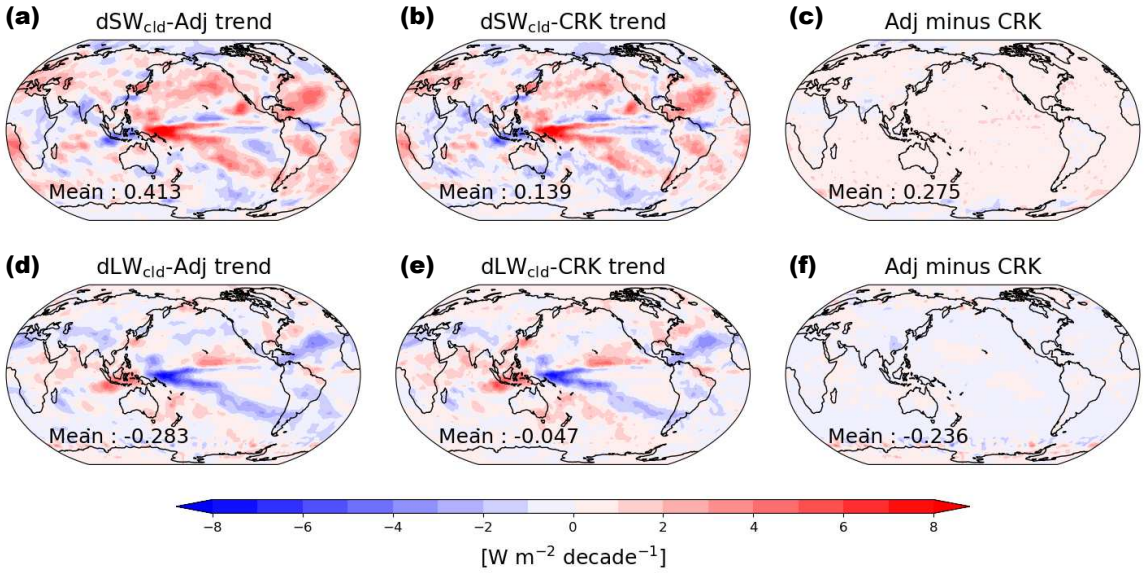


Figure 1. Spatial distributions of linear trends in the shortwave (dSW_{cld}) and longwave (dLW_{cld}) cloud radiative response over 2003–2022, derived using the adjustment (Adj) and cloud radiative kernel (CRK) methods. Trends in **(a)** dSW_{cld}-Adj and **(b)** dSW_{cld}-CRK, and **(c)** their difference (Adj minus CRK). **(d–f)** As in **(a–c)**, but for the dLW_{cld}. Global-mean values are reported in the lower-left corner of each map. Positive values indicate an increase in downward radiative response at the top of the atmosphere. In the shortwave, this corresponds to increased absorption (reduced reflection), whereas in the longwave it corresponds to reduced outgoing thermal radiation. Negative values indicate the opposite.

4.2. Insights from CMIP6 results

The relationship between dR_{cld}-Adj and dR_{cld}-CRK has been examined extensively in studies of cloud feedback under idealized forcing, such as increase in CO_2 concentration or prescribed sea surface temperature perturbations, where the two approaches are typically expected to yield comparable estimates of the cloud feedback (e.g., Zelinka et al. 2012a). Here, we extend this comparison to CMIP6 historical simulations and to trend analysis, where multiple forcings—including greenhouse gases, aerosols, and volcanic eruptions—evolve simultaneously, more closely resembling the observational record. Specifically, we evaluate consistency between the trends in dR_{cld}-Adj and dR_{cld}-CRK across nine independent 20-year windows beginning in 1855.

Figure 2 shows that, despite the complexity of the historical forcing environment, the two methods produce broadly consistent 20-year trends in both shortwave and longwave cloud radiative response across most periods. The multi-model mean for each window generally lies near the 1:1 line and within the two-sided 95% confidence envelope, indicating that dR_{cld}-Adj and dR_{cld}-CRK capture similar multidecadal variability in cloud radiative changes. Importantly, repeating the analysis with the alternative cloud radiative kernels from Z13 yields the same qualitative conclusions (Fig. S3) and brings the relationship into even closer agreement with the 1:1 line than the FBCT-based CRKs. This improvement may partly reflect differences in the underlying kernel construction and cloud-regime sensitivities between the two CRK products (Text S2).

A notable exception occurs for the 1975–1994 shortwave trend (Fig. 2a), during which the two methods diverge more strongly. This period includes the 1991 Mount Pinatubo eruption, which injected large amounts of sulfate aerosol into the stratosphere, increased planetary shortwave

reflection through aerosol scattering, and resulted in a pronounced transient cooling (e.g., Minnis et al., 1993; McCormick et al., 1995). During this period, dSW_{cld}-Adj exhibits a more negative trend than dSW_{cld}-CRK, reflecting the enhanced shortwave reflection associated with aerosols that is not attributable to cloud changes (Fig. S4). Because dSW_{cld}-Adj is diagnosed as a residual after removing kernel-estimated non-cloud contributions from dSWCRE, any incomplete removal of aerosol direct effects—which are not explicitly represented in the radiative kernel framework—can be aliased into the inferred cloud contribution. As a result, dSW_{cld}-Adj may become biased toward more negative values than dSW_{cld}-CRK during periods of strong aerosol forcing. Consistent with this interpretation, shifting the analysis window to exclude the Pinatubo period (e.g., 1971–1990) restores much closer agreement between the two estimates.

The observationally constrained estimates (red stars in Fig. 2), however, lie outside the model-derived 95% confidence envelope about the 1:1 line. Although this offset may appear analogous to the Pinatubo-related divergence in the shortwave, it is unlikely to be explained solely by differences in the treatment of aerosol–radiation interactions. In particular, the radiative-kernel-based adjustment estimate agrees closely with the PRP-based adjustment estimate (Fig. S2a), in which aerosol–radiation interactions are treated explicitly as a perturbing agent (Loeb et al., 2021; Loeb et al., 2025). This close agreement in the observed global-mean dSW_{cld}-Adj trends therefore suggests that the observational discrepancy in Fig. 2a cannot be attributed simply to whether aerosol direct effects are treated explicitly or diagnostically.

Moreover, aerosol trends are highly spatially heterogeneous, characterized by declining anthropogenic aerosol emissions in the Northern Hemisphere and increasing contributions from

natural aerosols in the Southern Hemisphere (Park and Soden, 2025). Given this pronounced heterogeneity, it is difficult to explain the difference between dSW_{cld}-Adj and dSW_{cld}-CRK as a near-uniform positive pattern. This contrast is especially evident when compared with the Pinatubo case, in which the radiative perturbation exhibits strong regional structure (Fig. S5).

The longwave divergence shown in Fig. 2b is even more difficult to explain in terms of a clear physical mechanism. Part of this divergence could reflect non-cloud contributions that are not fully excluded by the adjustment framework. This issue may be particularly important in the longwave, where the radiative response is more sensitive to water vapor and temperature, and thus to uncertainty in cloud-masking corrections. Nevertheless, the residual remains spatially coherent on global scales. Taken together, these results motivate further examination of potential observational uncertainties that could project onto satellite-era cloud radiative trends.

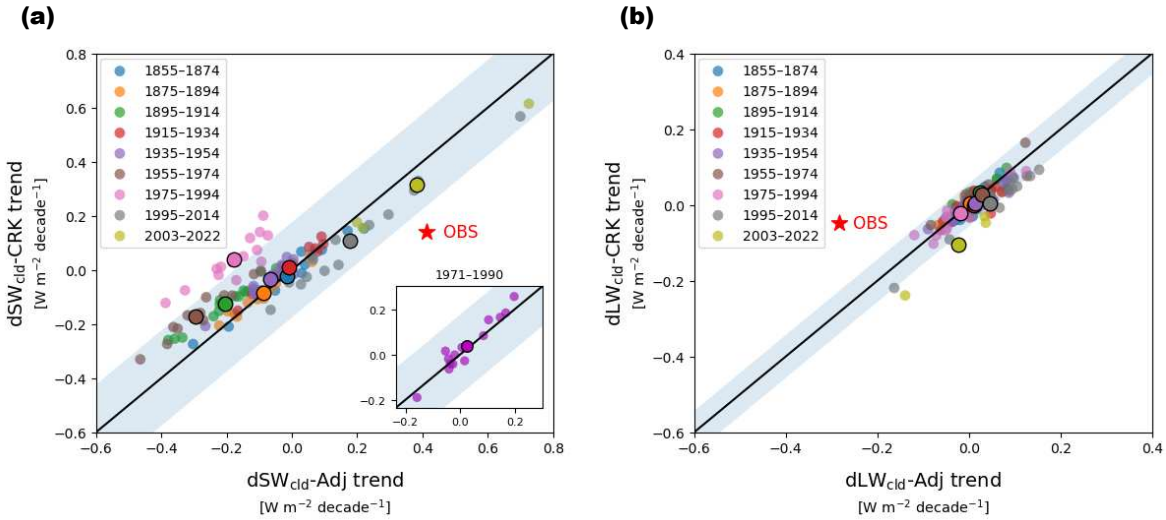


Figure 2. Comparison of 20-year trends in cloud radiative response from adjustment (dR_{cld}-Adj) and CRK (dR_{cld}-CRK) methods in CMIP6 historical simulations for (a) SW and (b) LW. Each scatter corresponds to a model, with colors indicating the 20-year analysis window spanning 1855–2014 (nine periods total). Black-outlined scatters denote the multi-model mean for

each period. The solid black line indicates the 1:1 relationship, and the blue shading shows the 95% confidence envelope about the 1:1 line. The red star marks the estimate derived from satellite observations (OBS) over 2003–2022. Note that for the 2003–2022 comparison, only three CMIP6 models provide the required variables (GFDL-CM4, HadGEM3-GC31-LL, and IPSL-CM6A-LR), whereas 14 models are available for the pre-2014 periods (Table S1). The inset in **(a)** shows the 1971–1990 period separately to illustrate the relationship when the analysis window excludes the 1991 Mount Pinatubo eruption. For consistency with the observational estimate, the same radiative kernels (Kramer et al., 2019) and the FBCT-derived cloud radiative kernels (Sun et al., 2022) are used.

4.3. Multiple Lines of Evidence for Drift in Satellite Measurements

4.3.1 Trends in the Cloud Radiative Kernels

A fundamental assumption underlying the cloud radiative kernel framework is that the kernel is time-invariant, representing a fixed radiative sensitivity of TOA flux to a unit change in cloud fraction for a given cloud type. Under this assumption, temporal changes in cloud radiative response should arise from changes in cloud properties, such as cloud fraction, optical depth, or vertical distribution, rather than from systematic changes in the kernel itself.

In the FBCT implementation, we diagnose temporal changes in the kernel by computing the time-varying anomalies in $(R^{ovc} - R^{clr})/100\%$ relative to the climatological-mean CRK, denoted dCRK. Figure 3a shows that trend in dSWCRK is weak but broadly positive values across much of the globe, consistent with a reduction in shortwave reflectance over overcast clouds, alongside

modest negative trends in a few regions (e.g., East Asia and the southeastern Pacific). Similarly, trends in dLWCRK is weak but broadly negative across much of the globe (Fig. 3e), implying that overcast clouds become less effective at reducing outgoing longwave radiation at the top of the atmosphere.

This pattern persists when the kernels are separated into low (CTP>680hPa), mid (680-440 hPa), and high (CTP<440 hPa) clouds (Fig. 3), indicating that the dCRK trends are not confined to a single cloud regime. In the shortwave, all three cloud categories show broadly similar positive spatial structures, suggesting that the kernel change is vertically widespread rather than layer specific. In the longwave, the interpretation is less straightforward because longwave cloud radiative fluxes, even under overcast conditions, are more sensitive to non-cloud influences such as atmospheric water vapor and temperature. Part of the diagnosed dLWCRK trends may therefore reflect these contributions, particularly because the FBCT CRKs are derived in the presence of observed surface and meteorological variations rather than under fixed surface and atmospheric conditions, as is more typical of conventional CRK construction (Text S2). Even so, broadly coherent negative kernel trends are found in all cloud regimes.

Figure S6 further shows that dSWCRK exhibits robust positive trends across nearly all cloud bins in CTP–COD space, with maximum values of approximately ~0.006 W m^{-2} $\%^{-1}$ $decade^{-1}$, whereas dLWCRK shows broadly negative trends, with magnitudes reaching about ~−0.022 W m^{-2} $\%^{-1}$ $decade^{-1}$. Although these trends are small in absolute magnitude in individual CTP−COD bin, they can still exert a substantial influence on the cloud radiative effect when multiplied by the climatological-mean cloud fraction. Following Oreopoulos et al. (2026), this can be illustrated by

expressing the cloud radiative effect in each bin as $\mathrm{CRE}_i \approx (\mathrm{R}_i^{\mathrm{ovc}} - \mathrm{R}_i^{\mathrm{clr}})/100\% \times \mathrm{CF}_i$. A first-order decomposition of anomalies about the climatological mean then gives

$$\mathrm{dCRE}_i \approx (\mathrm{CRK}_i \times \mathrm{dCF}_i) + (\mathrm{dCRK}_i \times \overline{\mathrm{CF}}_i), \qquad (5)$$

where i indexes the CTP–COD bins, dCF_i is the cloud fraction anomaly in each bin, and $\overline{\mathrm{CF}}_i$ is the climatological cloud fraction. Summing over all bins, the first term corresponds to $\mathrm{dR_{cld}}$-CRK by definition (Eq. 3), while the second term captures the contribution from temporal changes in the kernel itself (kernel-variability term). The covariance term $\mathrm{dCRK} \times \mathrm{dCF}$ is neglected because it has been shown to be negligible in similar analyses (Oreopoulos et al., 2026).

In our analysis, the kernel-variability term contributes 0.167 ± 0.051 W m^{-2} decade^{-1} in the shortwave (Fig. 4a), accounting for a larger fraction of the estimated dSWCRE trend of 0.309 ± 0.108 W m^{-2} decade^{-1} (Fig. 4b) than the first term, $\mathrm{dSW_{cld}}$-CRK (0.139 ± 0.099 W m^{-2} decade^{-1}), at the 95% confidence level. In the longwave, the kernel-variability term is even larger, reaching −0.417 ± 0.038 W m^{-2} decade^{-1}, and accounts for most of the estimated dLWCRE trend of −0.497 ± 0.073 W m^{-2} decade^{-1} (Fig. 4c,d). The spatial patterns of the kernel-variability term are also notable in being broadly coherent across much of the globe. By contrast, the more pronounced regional structure in the dCRE trends are more closely captured by the first term, $\mathrm{dR_{cld}}$-CRK (Fig. 1b,e versus Fig. 4b,d). This indicates that temporal changes in the kernel contribute primarily to the global-mean trends, whereas the spatial variability is more closely tied to changes in cloud properties represented by the CRK-based estimates. Thus, non-zero dCRK trends imply that part

of the inferred dCRE trends—and therefore part of residual-based dR_{cld}-Adj trends—may arise from changes in the kernel itself.

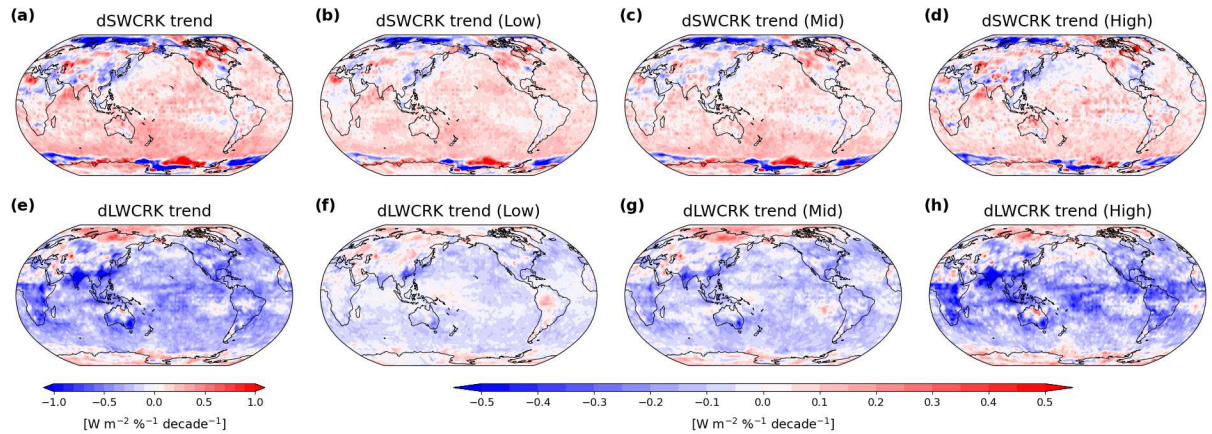


Figure 3. Spatial distributions of trends in dCRK over 2003–2022, separated by cloud top pressure. Trends in dSWCRK are shown for **(a)** all clouds, **(b)** low clouds (CTP>680hPa), **(c)** midlevel clouds (440-680hPa), and **(d)** high clouds (CTP<440hPa), respectively. **(e–h)** As in **(a–d)** but for dLWCRK. In the shortwave, positive values indicate that a given increase in cloud fraction produces less reflected shortwave radiation. In the longwave, negative values indicate that a given increase in cloud fraction produces a smaller reduction in outgoing longwave radiation.

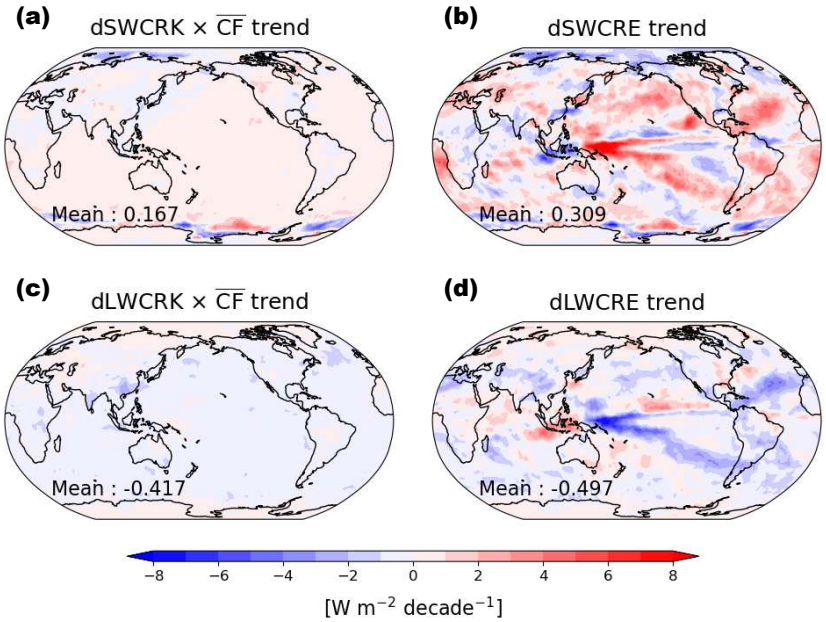


Figure 4. Spatial distributions of trends over 2003–2022 in the kernel-variability term and diagnosed cloud radiative effect. (a) Trend in the shortwave kernel-variability term, defined as dSWCRK × $\overline{CF}$ and **(b)** the trend in diagnosed shortwave cloud radiative effect, dSWCRE. **(c,d)** As in **(a,b),** but for the longwave component. Global-mean values are reported in the lower-left corner of each map.

4.3.2 Trends in Albedo Over Invariant Earth Targets and Their Radiative Imprint

Albedo diagnostics over invariant Earth targets provide an independent test of long-term radiometric stability. Deep convective clouds (DCCs), Libya-4, and Dome C are widely used Earth targets for assessing radiometric drifts. After removing the annual cycle, we find statistically significant negative trends in DCC albedo of −0.104 ± 0.075 % decade^{-1} for Terra and −0.213 ± 0.08 % decade^{-1} for Aqua over 2003–2022 (95% confidence; Fig. 5a). These estimates are consistent with Shankar et al. (2023), who reported −0.05 ± 0.08 % decade^{-1} for Terra and −0.15 ± 0.08 % decade^{-1} for Aqua over July 2002–July 2022. The negative DCC albedo trends indicate a small decrease in inferred reflectivity, consistent in sign with the dSWCRK trends diagnosed in

Section 4.3.1.

Figure 5c shows the Libya-4 results, and Fig. 5e shows the Dome C results. Both targets also exhibit consistently negative albedo trends, despite the more limited sampling associated with their small target size (20 km × 20 km). For Libya-4, the trends are -0.158 ± 0.083 % decade^{-1} for Terra and -0.271 ± 0.085 % decade^{-1} for Aqua (95% confidence). For Dome C, the corresponding trends are -0.160 ± 0.131 % decade^{-1} for Terra and -0.130 ± 0.122 % decade^{-1} for Aqua (95% confidence).

Although these fractional drifts may have been interpreted as negligible, even weak systematic changes in reflectance can project onto inferred shortwave radiative trends when accumulated globally over multi-decadal periods. This motivates further work to place the target-albedo trends on a radiative footing. In particular, we convert the observed fractional changes in target albedo into equivalent perturbations in reflected shortwave flux. As a first-order approximation, we assume that fractional changes in planetary reflectivity scale with the fractional changes inferred from target albedo. Under this assumption, the shortwave response associated with target albedo variability can be written as

$$\mathrm{dSW}_{\mathrm{target}} = \bar{Q} \times \bar{\alpha} \times \left(\frac{\mathrm{d}\alpha_{\mathrm{target}}}{\overline{\alpha_{\mathrm{target}}}} \right), \qquad (6)$$

where $\bar{Q}$ is the global-mean climatological incoming solar radiation at the top of the atmosphere ($\approx$340 W m^{-2}), and $\bar{\alpha}$ is the global-mean climatological planetary albedo ($\approx$0.29), both from CERES EBAF Edition 4.2. Here, $\mathrm{d}\alpha_{\mathrm{target}}$ denotes the monthly anomalies in target albedo, while $\overline{\alpha_{\mathrm{target}}}$ is the climatological mean target albedo. For Dome C, annual values are used because

observations are unavailable during polar night. Although dSW_{target} represents reflected shortwave response at the TOA, it is expressed here using the downward-positive sign convention.

The change in DCC albedo relative to its climatological mean, $d\alpha_{DCC}/\overline{\alpha_{DCC}}$, corresponds to a fractional reduction of about −0.002 ± 0.001 decade^{-1} for Terra and −0.003 ± 0.001 decade^{-1} for Aqua (95% confidence). Applying these small fractional changes to the global-mean reflected shortwave flux yields equivalent radiative perturbations of 0.150 ± 0.107 W m^{-2} decade^{-1} for Terra and 0.307 ± 0.115 W m^{-2} decade^{-1} for Aqua (Fig. 5b). Because the FBCT record combines Terra and Aqua observations, the corresponding mean estimate is approximately 0.229 W m^{-2} decade^{-1}. These back-of-the-envelope calculations are necessarily approximate, but they show that even very small long-term changes in reflectivity can produce radiative perturbations comparable in magnitude to the residual shortwave trend (0.275 W m^{-2} decade^{-1}) discussed in Section 4.1.

The radiative imprints inferred from Libya-4 and Dome C are also consistently positive. For Lybia-4, the estimated dSW_{target} trends are 0.443 ± 0.228 W m^{-2} decade^{-1} for Terra and 0.755 ± 0.235 W m^{-2} decade^{-1} for Aqua (95% confidence; Fig. 5d). For Dome C, the corresponding values are 0.231 ± 0.189 W m^{-2} decade^{-1} for Terra and 0.188 ± 0.176 W m^{-2} decade^{-1} for Aqua (95% confidence; Fig. 5f). The relatively larger values inferred from Libya-4 may partly reflect additional influences from atmospheric components, such as precipitable water, ozone, and aerosols, as discussed by Doelling et al. (2024). Overall, all three invariant Earth targets show the statistically significant negative albedo trends and imply positive radiative perturbations of comparable order of magnitude.

Importantly, Libya-4 and Dome C are clear-sky surface targets, whereas DCC is an overcast cloud target over ocean. The fact that all three exhibit negative albedo trends suggests that the signal is not unique to cloud scenes, but instead reflects a broader drift in CERES shortwave radiometry. Such drift could still affect shortwave cloud diagnostics, including SWCRE, which is defined as the difference between all-sky and clear-sky shortwave fluxes (downward positive). Although any drift common to both terms would partly cancel, scene-dependent differences between all-sky and clear-sky conditions could still project onto the dSWCRE trend.

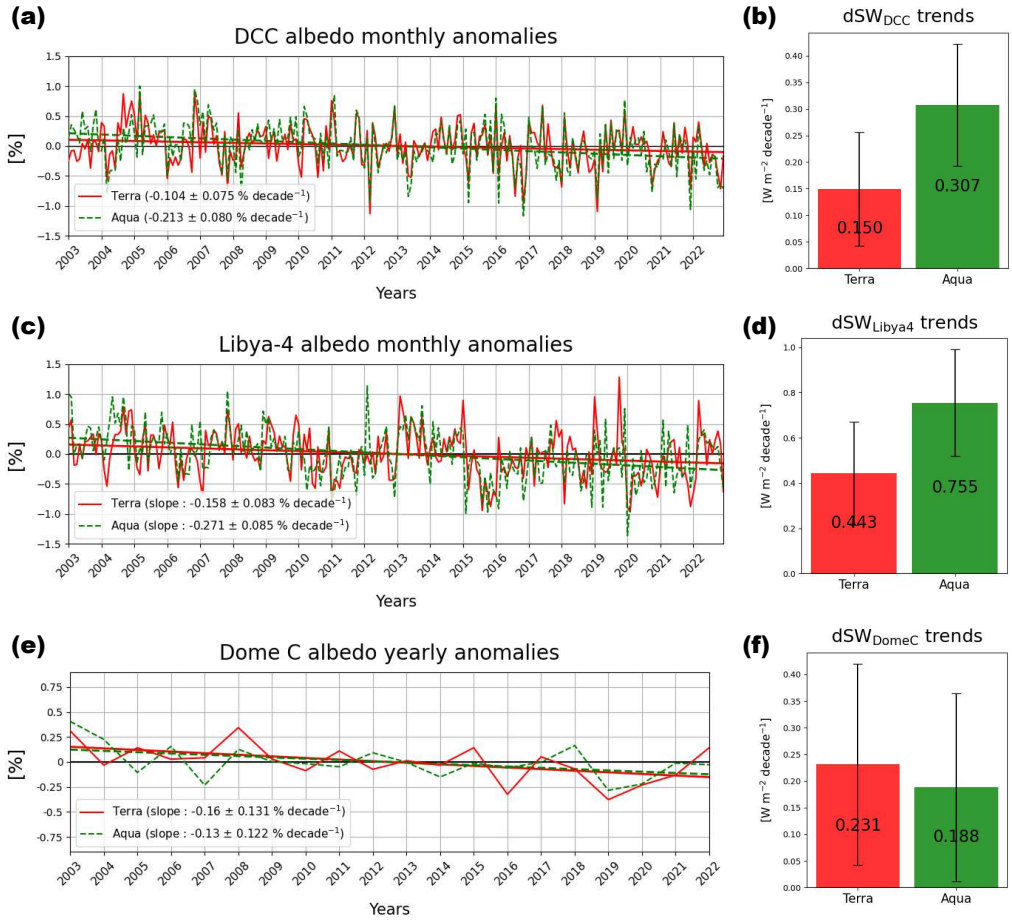


Figure 5. Albedo trends over invariant Earth targets and the corresponding implied reflected shortwave radiative trends. (a) Monthly anomalies in DCC albedo from CERES Terra (solid red) and Aqua (dashed green) over 2003–2022, with fitted linear trends. **(b)** Estimated reflected

shortwave radiative trends (downward-positive) associated with the observed DCC albedo changes. Uncertainties represent 95% confidence intervals. **(c, e)** Same as **(a)**, but for Libya-4 and Dome C, respectively. **(d, f)** Same as **(b)**, but for Libya-4 and Dome C, respectively.

4.3.3 Day–Night Longwave and Window-Channel TOA Flux Differences

Another independent diagnostic of possible radiometric drift is provided by day-minus-night differences in the LW and WN channels at TOA. During daytime, the CERES LW flux is derived as the difference between the TOT and SW channels, whereas during nighttime the LW flux is derived directly from the TOT channel. In contrast, the WN channel provides a more direct measure of longwave emission and is expected to capture any real diurnal-cycle changes in LW radiation. Comparing the day-minus-night differences in the LW and WN fluxes therefore provides a useful consistency check on possible drift in the SW channel or in the SW component of the TOT channel. In particular, we define the double difference as $\left(\mathrm{LW_{day}} - \mathrm{LW_{night}}\right) - \left(\mathrm{WN_{day}} - \mathrm{WN_{night}}\right)$, which should remain near zero if the daytime LW retrievals are stable relative to the WN channel. Using this diagnostic, Loeb et al. (2012) identified evidence of satellite drift during the first few years after launch.

Figure 6 shows the day-minus-night differences in the LW and WN TOA fluxes. The LW record exhibits a clear positive trend prior to June 2020 (0.106 ± 0.07 W m^{-2} decade^{-1} for Terra and 0.073 ± 0.08 W m^{-2} decade^{-1} for Aqua (95% confidence; Fig. 6a). Because outgoing longwave radiation is plotted here using the positive-upward sign convention, the positive LW trend is consistent in sign with a positive trend in downward shortwave radiative response. A pronounced drop is evident in both Terra and Aqua after May 2020, consistent with the issue noted by Shankar et al. (2023).

They reported that updates to the TOT channel spectral response functions (SRFs), which characterize the wavelength-dependent sensitivity of the instrument and are used to convert measured radiances into broadband TOA fluxes, were halted in May 2020, producing a detectable departure from the earlier long-term behavior. They further noted that this issue is expected to be addressed in Edition 5, which will restore monthly SRF updates. By contrast, the WN fluxes remain relatively stable over the full 20-year period (Fig. 6b).

To better isolate possible drift-related behavior, we examine the double difference (Fig. 7a). This quantity exhibits a statistically significant positive trend in both Terra and Aqua up to May 2020. Terra shows a trend of 0.149 ± 0.061 W m^{-2} decade^{-1}, while Aqua shows 0.129 ± 0.065 W m^{-2} decade^{-1} (95% confidence). These results indicate that, even before the discontinuation of monthly SRF updates, a small but statistically significant drift was already present. The positive pre-2020 trend in this diagnostic is therefore consistent with a positive drift in daytime SW flux and a negative daytime drift in LW flux under the downward-positive convention, in agreement with the independent radiometric stability diagnostics discussed in earlier sections. Over the full 2003–2022 period, Terra shows a trend of 0.239 ± 0.053 W m^{-2} decade^{-1}, while Aqua shows -0.039 ± 0.07 W m^{-2} decade^{-1} (95% confidence), reflecting the influence of the post-2020 discontinuity. Nevertheless, Terra still exhibits a statistically significant positive trend.

The spatial pattern of this diagnostic is broadly consistent with previous CERES calibration analyses, with positive trends over many land and extratropical regions and weaker or negative trends over the tropics and subtropics (Fig. 7b,c). Loeb et al. (2016) likewise reported pronounced positive trends in the double difference over the Saharan desert and explained that they most likely

reflect errors in the daytime shortwave retrieval. The strong positive anomalies over bright desert surfaces further suggest that the large positive radiative imprint inferred from Libya-4 in Section 4.3.2 may also reflect calibration-related drift associated with shortwave radiometry, in addition to atmospheric influences on the target itself.

Although these diagnostics cannot be compared directly in magnitude with cloud radiative trend estimates, because they involve different quantities, they nevertheless provide clear evidence of drift in the satellite radiative record. This is especially relevant for FBCT, which relies exclusively on daytime fluxes and may therefore be particularly sensitive to such drift. These results therefore provide further support for the interpretation that subtle radiometric instability may project onto satellite-era cloud radiative trends.

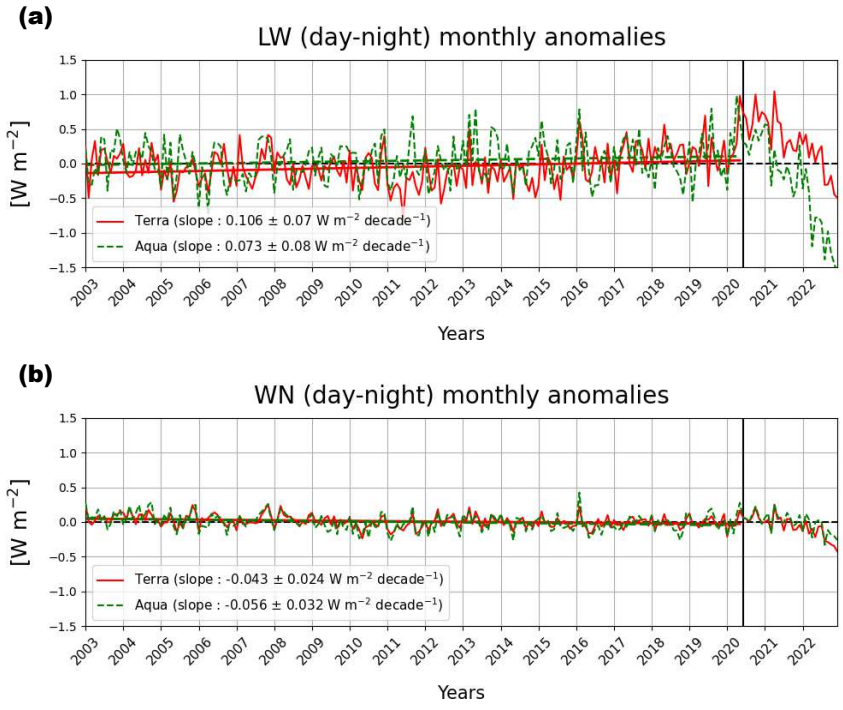


Figure 6. Global-mean monthly anomalies in daytime-minus-nighttime TOA radiative fluxes over 2003–2022 for (a) LW and (b) WN TOA fluxes. Red solid lines denote Terra, and green

dashed lines denote Aqua. The vertical black line marks May 2020, when the spectral response function updates were halted; linear trends fitted through that date are shown, with uncertainties indicating the 95% confidence interval.

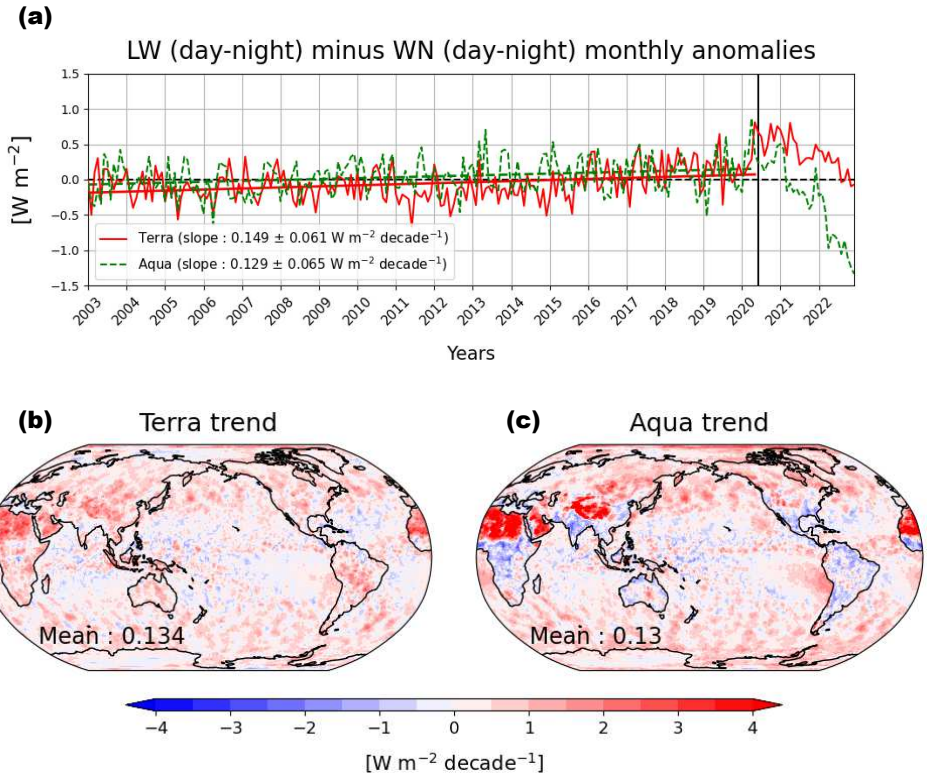


Figure 7. Trends in the difference between daytime-minus-nighttime LW and WN TOA fluxes. **(a)** Global-mean monthly anomalies in LW (day–night) minus WN (day–night) for Terra (red solid) and Aqua (green dashed) over 2003–2022. The vertical black line marks May 2020, when the spectral response function updates were halted; linear trends fitted through that date are shown, with uncertainties indicating the 95% confidence interval. Spatial distribution of the linear trend in LW (day–night) minus WN (day–night) over January 2003–May 2020 for **(b)** Terra and **(c)** Aqua. Global-mean values are reported in the lower-left corner of each map. Small differences

675 between the global-mean trends in **(a)** and those for the corresponding satellites in **(b,c)** arise from
676 missing daytime and nighttime retrievals over high-latitude regions.
677

678 **4.4. Implications for Net Cloud Radiative Trends and Earth's Energy Imbalance Trends**
679 Multiple lines of evidence presented in Section 4.3 point to subtle but statistically significant drift
680 in the satellite radiative record. Although small in absolute magnitude, such drifts can become
681 radiatively important if they project onto cloud radiative effect and, in turn, onto adjustment-based
682 cloud radiative response. The CRK-based estimates, by contrast, appear less sensitive to these
683 drifts and therefore provide a useful benchmark for isolating the physically meaningful cloud
684 signal. In this section, we further interpret these findings by comparing the observations with
685 model-simulated cloud radiative trends and by examining their implications for recent changes in
686 Earth's energy imbalance.
687

688 Because the adjustment and CRK frameworks are broadly consistent across multiple 20-year
689 periods in the CMIP6 historical simulations (Section 4.2), we use adjustment-based estimates from
690 a larger sample of 44 CMIP6 models over 2003–2022 (Table S1) as a benchmark for evaluating
691 the observed trends. Figure 8a compares the observed cloud radiative trends with the model-
692 simulated distributions in the shortwave, longwave, and net. In the shortwave, the adjustment-
693 based estimate falls near the edge of the one-standard-deviation range, whereas the CRK-based
694 estimate lies closer to the multi-model mean. Even so, both remain within the overall model spread,
695 suggesting that the magnitude of the observed shortwave cloud trend is not unusual relative to the
696 range of internal variability and forced responses simulated by the models. In contrast, the
697 observed longwave cloud radiative trend derived from adjustment method lies well outside the

model range. This indicates that the observed longwave trend from adjustment method is not only large in magnitude, but also difficult to reconcile with the cloud radiative trends simulated by models. In comparison, the CRK-based longwave estimate, as in the shortwave, shows substantially better agreement with the model-simulated distribution.

The implications for the net cloud radiative trend are particularly noteworthy. As discussed in Section 4.1, the residuals between the adjustment- and CRK-based cloud radiative trends are similar in magnitude but opposite in sign in the shortwave and longwave (0.275 W m^{-2} $decade^{-1}$ versus −0.236 W m^{-2} $decade^{-1}$). Section 4.3.3 further suggests that part of the daytime longwave drift may arise from the same shortwave-related bias, thereby producing compensating errors between the two components. As a result, the net cloud radiative trends remain relatively insensitive to the choice of observational method: the adjustment- and CRK-based estimates are both close to the model mean and lie within approximately one standard deviation of the model distribution (Fig. 8a). This suggests that observational uncertainty primarily affects the partitioning of the cloud radiative trend into its shortwave and longwave components, while having a much smaller influence on the net cloud radiative response.

A similar conclusion emerges for the all-sky TOA radiative flux trends (Fig. 8b). The observed shortwave TOA flux trend is larger than the model mean, but after applying the residual-based adjustment, the revised estimate shifts closer to the mean of the model distribution. In the longwave, the original observational estimate lies outside the one-standard-deviation range of the models, whereas the revised estimate falls well within the model spread. By comparison, the change in the net TOA radiative trend is much smaller, because the shortwave and longwave adjustments largely

offset one another. Thus, these results suggest that accounting for subtle radiometric drift substantially reconciles the observed and simulated shortwave and longwave radiative trends, while leaving the net radiative imbalance comparatively unchanged.

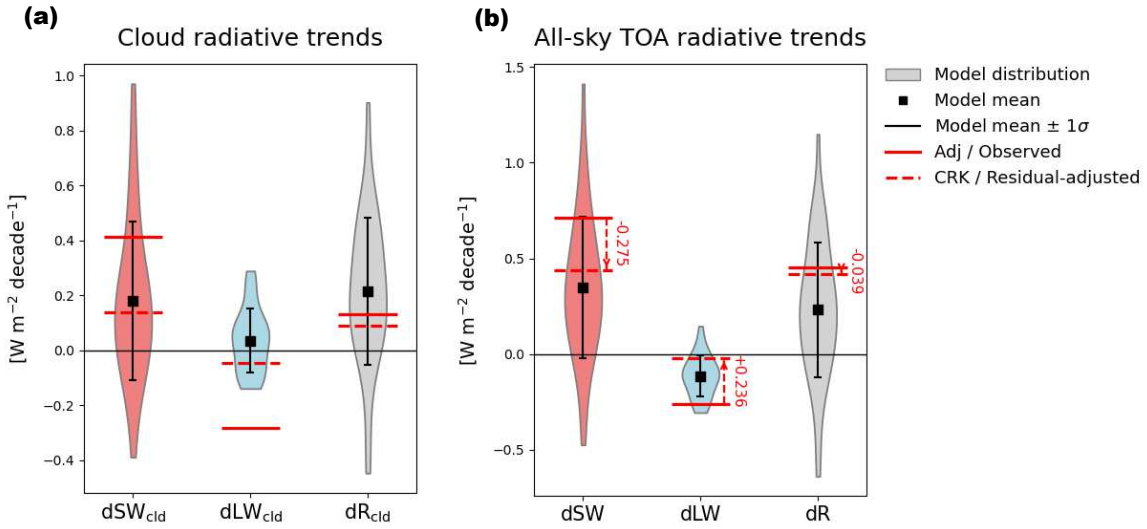


Figure 8. Distribution of model-simulated and observed radiative trends over 2003–2022 for cloud radiative responses and all-sky TOA fluxes. (a) Trends in shortwave, longwave, and net cloud radiative responses (dSW_{cld}, dLW_{cld}, and dR_{cld}) from 44 CMIP6 models, diagnosed using the adjustment-based framework. **(b)** Corresponding model distributions for all-sky TOA shortwave, longwave, and net radiative flux trends (dSW, dLW, and dR). Violin plots show the model distributions, black squares denote the multi-model mean, and black vertical lines indicate $\pm 1\sigma$ about the model mean. In **(a)**, red solid and dashed lines denote the observational estimates derived from the adjustment (Adj) and CRK frameworks, respectively. In **(b)**, red solid lines denote the observational estimates from CERES EBAF Edition 4.2, and the red dashed lines denote the residual-adjusted estimates using the Adj–CRK differences shown in **(a)**. Red numerical annotations indicate the magnitudes of the applied residual adjustments.

5. Conclusions and Discussion

This study examines the origin of the apparent discrepancy between observed and model-simulated cloud radiative trends inferred from the adjustment method and revisits the recent cloud radiative contribution to Earth's energy imbalance (EEI) using an independent cloud radiative kernel (CRK) framework. We find that, although the CRK approach reproduces the broad spatial patterns and temporal variability of the adjustment-based estimates, it explains only a limited fraction of their global-mean shortwave and longwave trends over 2003–2022. The resulting residual is spatially widespread, positive in the shortwave, and negative in the longwave, a structure that is difficult to explain by physically plausible cloud changes alone. Multiple independent diagnostics—including trends in the cloud radiative kernels themselves, albedo changes over invariant Earth targets, and trends in daytime-minus-nighttime longwave and window-channel fluxes—consistently point to subtle but non-negligible radiometric drift in the satellite record. These results suggest that part of the apparent model–observation discrepancy in recent shortwave and longwave cloud radiative trends may arise from subtle observational drift, while the net cloud radiative contribution to EEI remains comparatively robust.

This interpretation does not imply that the adjustment-based framework is without value. Rather, it suggests that interpreting adjustment-based trends requires careful assessment of observational stability, particularly when the inferred signal is decomposed into separate shortwave and longwave components. Uncertainty in satellite cloud retrievals also remains an important caveat, since the CRK-based framework depends on observed changes in cloud fraction across CTP–COD bins. While such uncertainties may influence the magnitude and regional structure of CRK-based trends, they do not readily explain the broad, compensating shortwave and longwave residual

patterns documented here. In this sense, the adjustment and CRK approaches should be viewed as complementary: the adjustment framework remains useful for diagnosing total cloud radiative changes from observed TOA fluxes, while the CRK framework helps relate those radiative changes to observed changes in cloud-type distributions.

The implications also extend to recent attempts to use the observed shortwave and longwave trends to constrain equilibrium climate sensitivity (ECS). For example, Myhre et al. (2025) argued that the observed combination of strong positive shortwave and negative longwave trends may provide a constraint against the low-ECS models. By contrast, our results suggest that, once the residual biases identified here are taken into account, the adjusted SW and LW trends may be more consistent with the range of model-simulated behavior, including that of some lower-ECS models. This perspective aligns with the motivation of CERESMIP (Schmidt et al., 2023), which was proposed to assess the CERES-era EEI trend and its shortwave and longwave components using updated forcings and observed sea surface temperatures, while recognizing that agreement between models and observations is generally better for the net EEI trend than for its shortwave and longwave components considered separately. These findings highlight that interpreting the observed shortwave and longwave contributions to recent EEI trends requires not only physically based diagnostics but also careful evaluation of subtle observational uncertainties.

Acknowledgments

We are grateful to Dr. Norman Loeb for sharing the PRP-based dR_{cld}-Adj estimate described in Loeb et al. (2025). We also thank Dr. Norman Loeb, Dr. Lazaros Oreopoulos, and Dr. Ryan Kramer for insightful discussions and constructive comments, and Nayeong Cho and Dr. Dongmin

Lee for helpful discussions. This work was supported by the National Aeronautics and Space Administration (NASA) under Grant 80NSSC23K0115 and Grant 80NSSC24M0014.

Data Availability Statement

CERES data (EBAF and FBCT) were obtained from NASA's CERES data portal and ordering tools (https://ceres.larc.nasa.gov/data/). Level-2 CERES SSF data used to identify deep convective cloud (DCC) targets were obtained from the NASA LaRC OPeNDAP server (https://opendap.larc.nasa.gov/opendap/CERES/SSF/contents.html). ERA5 reanalysis data were accessed via the Copernicus Climate Data Store (https://cds.climate.copernicus.eu/datasets). GISTEMP v4 surface temperature data were obtained from NASA GISS (https://data.giss.nasa.gov/gistemp/). CMIP6 model output used in this study is available through the Earth System Grid Federation (ESGF) data portal (https://esgf-node.llnl.gov/projects/esgf-llnl/). The ensemble-mean estimate used in the Introduction is taken from Raghuraman et al. (2023) and is available on Zenodo (https://doi.org/10.5281/zenodo.4784726; Raghuraman et al., 2021b). The PRP-based estimate from Loeb et al. (2025) is available from the CERES PRP anomalies archive (https://ceres.larc.nasa.gov/data/ceres-prp-anomalies-2025/). The Zhou et al. (2013) cloud radiative kernels used here are available via the cloud radiative kernel archive maintained by Zelinka (2021) on Zenodo (https://doi.org/10.5281/zenodo.5514137).

Conflict of Interest Disclosure

The authors declare there are no conflicts of interest for this manuscript.

References

Chao, L.-W., Zelinka, M. D., & Dessler, A. E. (2024). Evaluating Cloud Feedback Components in Observations and Their Representation in Climate Models. *Journal of Geophysical Research: Atmospheres*, *129*(2), e2023JD039427. https://doi.org/10.1029/2023JD039427

Doelling, D. R., Haney, C., Khakurel, P., Bhatt, R., Scarino, B., & Gopalan, A. (2024). Advanced Libya-4 radiometric and atmospheric characterization utilizing moderate resolution imaging spectroradiometer and visible infrared imaging radiometer suite full-scan reflective solar band measurements. *Journal of Applied Remote Sensing*, *18*(3), 034511. https://doi.org/10.1117/1.JRS.18.034511

Doelling, D. R., Wu, A., Xiong, X., Scarino, B. R., Bhatt, R., Haney, C. O., et al. (2015). The Radiometric Stability and Scaling of Collection 6 Terra- and Aqua-MODIS VIS, NIR, and SWIR Spectral Bands. *IEEE Transactions on Geoscience and Remote Sensing*, *53*(8), 4520–4535. https://doi.org/10.1109/TGRS.2015.2400928

Goessling, H. F., Rackow, T., & Jung, T. (2025). Recent global temperature surge intensified by record-low planetary albedo. *Science*, *387*(6729), 68–73. https://doi.org/10.1126/science.adq7280

Hersbach, H., Bell, B., Berrisford, P., Hirahara, S., Horányi, A., Muñoz-Sabater, J., et al. (2020). The ERA5 global reanalysis. *Quarterly Journal of the Royal Meteorological Society*, *146*(730), 1999–2049. https://doi.org/10.1002/qj.3803

Kramer, R. J., He, H., Soden, B. J., Oreopoulos, L., Myhre, G., Forster, P. M., & Smith, C. J. (2021). Observational Evidence of Increasing Global Radiative Forcing. *Geophysical Research Letters*, *48*(7), e2020GL091585. https://doi.org/10.1029/2020GL091585

826 Kramer, R. J., Matus, A. V., Soden, B. J., & L'Ecuyer, T. S. (2019). Observation-Based Radiative
827 Kernels From CloudSat/CALIPSO. *Journal of Geophysical Research: Atmospheres*, *124*(10),
828 5431–5444. https://doi.org/10.1029/2018JD029021
829 Lenssen, N. J. L., Schmidt, G. A., Hansen, J. E., Menne, M. J., Persin, A., Ruedy, R., & Zyss, D.
830 (2019). Improvements in the GISTEMP Uncertainty Model. *Journal of Geophysical Research:*
831 *Atmospheres*, *124*(12), 6307–6326. https://doi.org/10.1029/2018JD029522
832 Loeb, N. G. (2025). CERES Partial Radiative Perturbation Analysis Results 2025 [Dataset].
833 CERES PRP archive. https://ceres.larc.nasa.gov/data/ceres-prp-anomalies-2025/
834 Loeb, N. G., Doelling, D. R., Kato, S., Su, W., Mlynczak, P. E., & Wilkins, J. C. (2024). Continuity
835 in Top-of-Atmosphere Earth Radiation Budget Observations. https://doi.org/10.1175/JCLI-D-24-
836 0180.1
837 Loeb, N. G., Doelling, D. R., Wang, H., Su, W., Nguyen, C., Corbett, J. G., et al. (2018). Clouds
838 and the Earth's Radiant Energy System (CERES) Energy Balanced and Filled (EBAF) Top-of-
839 Atmosphere (TOA) Edition-4.0 Data Product. https://doi.org/10.1175/JCLI-D-17-0208.1
840 Loeb, N. G., Johnson, G. C., Thorsen, T. J., Lyman, J. M., Rose, F. G., & Kato, S. (2021). Satellite
841 and Ocean Data Reveal Marked Increase in Earth's Heating Rate. *Geophysical Research Letters*,
842 *48*(13), e2021GL093047. https://doi.org/10.1029/2021GL093047
843 Loeb, N. G., Kato, S., Su, W., Wong, T., Rose, F. G., Doelling, D. R., et al. (2012). Advances in
844 Understanding Top-of-Atmosphere Radiation Variability from Satellite Observations. *Surveys in*
845 *Geophysics*, *33*(3), 359–385. https://doi.org/10.1007/s10712-012-9175-1
846 Loeb, N. G., Manalo-Smith, N., Su, W., Shankar, M., Thomas, S., Loeb, N. G., et al. (2016).
847 CERES Top-of-Atmosphere Earth Radiation Budget Climate Data Record: Accounting for in-
848 Orbit Changes in Instrument Calibration. *Remote Sensing*, *8*(3). https://doi.org/10.3390/rs8030182

Loeb, N. G., Thorsen, T. J., Kato, S., Rose, F. G., Hodnebrog, Ø., & Myhre, G. (2025). Emerging hemispheric asymmetry of Earth's radiation. *Proceedings of the National Academy of Sciences*, *122*(40), e2511595122. https://doi.org/10.1073/pnas.2511595122

Mauritsen, T., Tsushima, Y., Meyssignac, B., Loeb, N. G., Hakuba, M., Pilewskie, P., et al. (2025). Earth's Energy Imbalance More Than Doubled in Recent Decades. *AGU Advances*, *6*(3), e2024AV001636. https://doi.org/10.1029/2024AV001636

McCormick, M. P., Thomason, L. W., & Trepte, C. R. (1995). Atmospheric effects of the Mt Pinatubo eruption. *Nature*, *373*(6513), 399–404. https://doi.org/10.1038/373399a0

Minnis, P., Harrison, E. F., Stowe, L. L., Gibson, G. G., Denn, F. M., Doelling, D. R., & Smith, W. L. (1993). Radiative Climate Forcing by the Mount Pinatubo Eruption. *Science*, *259*(5100), 1411–1415. https://doi.org/10.1126/science.259.5100.1411

Minnis, Patrick, Sun-Mack, S., Young, D. F., Heck, P. W., Garber, D. P., Chen, Y., et al. (2011). CERES Edition-2 Cloud Property Retrievals Using TRMM VIRS and Terra and Aqua MODIS Data—Part I: Algorithms. *IEEE Transactions on Geoscience and Remote Sensing*, *49*(11), 4374–4400. https://doi.org/10.1109/TGRS.2011.2144601

Myhre, G., Hodnebrog, Ø., Loeb, N., & Forster, P. M. (2025). Observed trend in Earth energy imbalance may provide a constraint for low climate sensitivity models. *Science*, *388*(6752), 1210–1213. https://doi.org/10.1126/science.adt0647

Ongoing changes in Terra and Aqua orbits impacting MODIS snow and sea ice products, National Snow and Ice Data Center. https://nsidc.org/data/user-resources/data-announcements/ongoing-changes-terra-and-aqua-orbits-impacting-modis-snow-and-sea-ice-products.

Oreopoulos, L., Cho, N., Kramer, R., Lee, D., Matus, A. (2026). Cloud radiative effect variability in the recent satellite record and associated cloud feedback [Preprint]. *ESS Open Archive*. https://doi.org/10.22541/essoar.177100425.52102553/v1

Park, C., & Soden, B. J. (2025). Negligible contribution from aerosols to recent trends in Earth's energy imbalance. *Science Advances*, *11*(48), eadv9429. https://doi.org/10.1126/sciadv.adv9429

Raghuraman, S. P., Paynter, D., & Ramaswamy, V. (2021). Anthropogenic forcing and response yield observed positive trend in Earth's energy imbalance. *Nature Communications*, *12*(1), 4577. https://doi.org/10.1038/s41467-021-24544-4

Raghuraman, S. P., Paynter, D., & Ramaswamy, V. (2021). Anthropogenic forcing and response yield observed positive trend in Earth's energy imbalance [Dataset]. Zenodo. https://zenodo.org/records/4784726

Raghuraman, S. P., Paynter, D., Menzel, R., & Ramaswamy, V. (2023). Forcing, Cloud Feedbacks, Cloud Masking, and Internal Variability in the Cloud Radiative Effect Satellite Record. *Journal of Climate*, *36*(12), 4151–4167. https://doi.org/10.1175/JCLI-D-22-0555.1

Rossow, W. B., & Schiffer, R. A. (1999). Advances in Understanding Clouds from ISCCP. Retrieved from https://journals.ametsoc.org/view/journals/bams/80/11/1520-0477_1999_080_2261_aiucfi_2_0_co_2.xml

Schmidt, G. A., Andrews, T., Bauer, S. E., Durack, P. J., Loeb, N. G., Ramaswamy, V., et al. (2023). CERESMIP: a climate modeling protocol to investigate recent trends in the Earth's Energy Imbalance. *Frontiers in Climate*, *5*. https://doi.org/10.3389/fclim.2023.1202161

Shankar, M., Loeb, N. G., Smith, N., Smith, N., Daniels, J. L., Thomas, S., & Walikainen, D. (2023). Evaluating the Radiometric Performance of the Clouds and the Earth's Radiant Energy

892 System (CERES) Instruments on Terra and Aqua Over 20 Years. *IEEE Transactions on*
893 *Geoscience and Remote Sensing*, *61*, 1–11. https://doi.org/10.1109/TGRS.2023.3330398
894 Soden, B. J., & Held, I. M. (2006). An Assessment of Climate Feedbacks in Coupled Ocean–
895 Atmosphere Models. https://doi.org/10.1175/JCLI3799.1
896 Soden, B. J., Held, I. M., Colman, R., Shell, K. M., Kiehl, J. T., & Shields, C. A. (2008).
897 Quantifying Climate Feedbacks Using Radiative Kernels. *Journal of Climate*, *21*(14), 3504–3520.
898 https://doi.org/10.1175/2007JCLI2110.1
899 Stephens, G. L., Hakuba, M. Z., Kato, S., Gettelman, A., Dufresne, J.-L., Andrews, T., et al.
900 (2022). The changing nature of Earth's reflected sunlight. *Proceedings of the Royal Society A:*
901 *Mathematical, Physical and Engineering Sciences*, *478*(2263), 20220053.
902 https://doi.org/10.1098/rspa.2022.0053
903 Sun, M., Doelling, D. R., Loeb, N. G., Scott, R. C., Wilkins, J., Nguyen, L. T., & Mlynczak, P.
904 (2022). Clouds and the Earth's Radiant Energy System (CERES) FluxByCldTyp Edition 4 Data
905 Product. https://doi.org/10.1175/JTECH-D-21-0029.1
906 Thorsen, T. J., Kato, S., Loeb, N. G., & Rose, F. G. (2018). Observation-Based Decomposition of
907 Radiative Perturbations and Radiative Kernels. https://doi.org/10.1175/JCLI-D-18-0045.1
908 von Schuckmann, K., Palmer, M. D., Trenberth, K. E., Cazenave, A., Chambers, D., Champollion,
909 N., et al. (2016). An imperative to monitor Earth's energy imbalance. *Nature Climate Change*,
910 *6*(2), 138–144. https://doi.org/10.1038/nclimate2876
911 Wetherald, R. T., & Manabe, S. (1988). Cloud Feedback Processes in a General Circulation Model.
912 Retrieved from https://journals.ametsoc.org/view/journals/atsc/45/8/1520-
913 0469_1988_045_1397_cfpiag_2_0_co_2.xml

Wu, A., Xiong, X., Doelling, D. R., Morstad, D., Angal, A., & Bhatt, R. (2013). Characterization of Terra and Aqua MODIS VIS, NIR, and SWIR Spectral Bands' Calibration Stability. *IEEE Transactions on Geoscience and Remote Sensing*, *51*(7), 4330–4338. https://doi.org/10.1109/TGRS.2012.2226588

Yue, Q., Kahn, B. H., Fetzer, E. J., Schreier, M., Wong, S., Chen, X., & Huang, X. (2016). Observation-Based Longwave Cloud Radiative Kernels Derived from the A-Train. https://doi.org/10.1175/JCLI-D-15-0257.1

Zelinka, M. D. (2021). mzelinka/cloud-radiative-kernels [Dataset]. Zenodo. https://zenodo.org/records/5514137

Zelinka, M. D., Klein, S. A., & Hartmann, D. L. (2012a). Computing and Partitioning Cloud Feedbacks Using Cloud Property Histograms. Part I: Cloud Radiative Kernels. https://doi.org/10.1175/JCLI-D-11-00248.1

Zelinka, M. D., Klein, S. A., & Hartmann, D. L. (2012b). Computing and Partitioning Cloud Feedbacks Using Cloud Property Histograms. Part II: Attribution to Changes in Cloud Amount, Altitude, and Optical Depth. https://doi.org/10.1175/JCLI-D-11-00249.1

Zelinka, M. D., Zhou, C., & Klein, S. A. (2016). Insights from a refined decomposition of cloud feedbacks. *Geophysical Research Letters*, *43*(17), 9259–9269. https://doi.org/10.1002/2016GL069917

Zhang, Y., Jin, Z., & Sikand, M. (2021). The Top-of-Atmosphere, Surface and Atmospheric Cloud Radiative Kernels Based on ISCCP-H Datasets: Method and Evaluation. *Journal of Geophysical Research: Atmospheres*, *126*(24), e2021JD035053. https://doi.org/10.1029/2021JD035053

Zhou, C., Zelinka, M. D., Dessler, A. E., & Yang, P. (2013). An Analysis of the Short-Term Cloud Feedback Using MODIS Data. https://doi.org/10.1175/JCLI-D-12-00547.1

Supplementary Files

This is a list of supplementary files associated with this preprint. Click to download.

- AGUSpplementaryinitialsubmission.docx